ADVANCED FUNCTIONAL MATERIALS
www.afm-journal.de

Room Temperature Pulsed Laser Deposition of Aluminum Zinc Oxide (AZO): Enabling Scalable Indium-Free Transparent Conductive Oxides

Joost W. C. Reinders, Jons Bolding, Cristina Roldán-Carmona, Federico Ventosinos, Abhyuday Paliwal, Lidón Gil-Escrig, Francisco Palazon, Michele Sessolo, Kassio P. S. Zanoni, and Henk J. Bolink**

Indium tin oxide (ITO) is the leading transparent electrode material in displays and in photovoltaics. As both these markets are vast and rapidly expanding, the demand for alternative transparent conductive oxides (TCOs) is becoming increasingly urgent due to the limited availability of indium. Herein, aluminum-doped zinc oxide (AZO) is revisited as a promising indium-free TCO candidate. An industrial-scale pulsed laser deposition (PLD) process is developed that produces highly conductive and transparent AZO films at room temperature, without the need for post-deposition annealing. This PLD-AZO films have excellent morphological, electrical, and optical properties, with sheet resistances of ≈ 55–25 Ω Υ^{-1} for thin TCO thicknesses (around 100 to 200 nm, respectively), and absorptance from 400 to 1000 nm below 10%. We demonstrate the application of this highly conductive PLD-AZO not only as a bottom contact but also as an effective top contact in perovskite solar cells, highlighting its versatility. The AZO-based devices achieve performance and stabilities equivalent to that of ITO-based. This findings demonstrate the robustness and potential of PLD-deposited AZO layers in enhancing displays and PV production and facilitating the wider adoption of renewable and sustainable TCO alternatives in the expanding photovoltaics and displays markets.

1. Introduction

Transparent conductive oxides (TCOs) are fundamental to the advancement of modern technologies, serving as essential components in both photovoltaic (PV) devices and display technologies.[1–3] Indium tin oxide (ITO) has long been the dominant TCO, favored for its exceptional combination of transparency and electrical conductivity. The primary market for ITO is in displays, a sector that is vast and continuously expanding. Simultaneously, the PV industry is experiencing rapid growth, driven by the deployment of silicon heterojunction (SHJ) technologies [4,5] and the anticipated rise of thin-film photovoltaics.[2,6–10] However, the finite and rapidly depleting supply of indium poses a significant threat to the sustainability and scalability of these critical technologies.[11,12] Current projections indicate that indium reserves could be exhausted within the next two decades, jeopardizing not only the future of display technologies but also the ability of PV systems to scale up,[13] in alignment with global climate objectives, such as those outlined in the Paris Agreement.[14] This growing demand across multiple industries underscores the urgent need to identify and integrate sustainable alternatives to ITO, ensuring the continued progress and widespread adoption of both PV and display technologies.

One such alternative, fluorine-doped tin oxide (FTO), has been explored but is constrained by the stringent deposition conditions required to achieve optimal electrical and optical properties, especially the high temperatures.[15,16] This limits its applicability to temperature stable substrates (generally glass) and, in solar cell applications, hinders its use as the top electrode in substrate configuration,[17–21] in semitransparent/bifacial devices[22,23] and in tandem solar cells.[24–28] Additionally, decreasing the sheet resistance of FTO-coated substrates often compromises transparency, leading to increased parasitic absorption.

Another indium-free TCO that has garnered significant attention is aluminum-doped zinc oxide (AZO), known for its

J. W. C. Reinders, J. Bolding, C. Roldán-Carmona, F. Ventosinos, A. Paliwal, L. Gil-Escrig, M. Sessolo, K. P. S. Zanoni, H. J. Bolink
Instituto de Ciencia Molecular
Universidad de Valencia
Calle Catedrático José Beltrán 2, Paterna 46980, Spain
E-mail: kasza@uv.es; henk.bolink@uv.es
F. Palazon
Departamento de Ingeniería Química y Ambiental
Universidad Politécnica de Cartagena
Plaza Cronista Isidro Valverde, Cartagena 30202, Spain

The ORCID identification number(s) for the author(s) of this article can be found under https://doi.org/10.1002/adfm.202418069

DOI: 10.1002/adfm.202418069

cost-effectiveness, abundance, and non-toxicity compared to ITO. AZO has been extensively studied as a promising alternative, but several challenges have hindered its widespread implementation. While AZO films with thicknesses up to 150 nm can typically achieve transmittances exceeding 80%, their conductivity is highly thickness-dependent, often resulting in non-uniform conductivity across the film. Moreover, AZO's stability under damp heat conditions is a concern, as it tends to degrade, limiting its long-term reliability in real-world applications. Achieving low resistivities in AZO films—typically no more than 1.3×10^5 S m^{-1} (or, no less than 8.0×10^{-4} Ω·cm)[29] for films with approx. 150 nm thick—has proven difficult without subjecting the material to harsh deposition conditions or post-deposition treatment with annealing at temperatures of at least 200 °C. These requirements complicate the use of AZO, especially when working with temperature-sensitive substrates or applications where homogeneity and long-term stability are critical. At room temperature, high conductivity in AZO has typically been attainable through pulsed laser deposition (PLD).[30–32] PLD is known for its precision and ability to create high-quality films with excellent morphological, electrical, and optical properties. However, for many years, PLD was considered unsuitable for large-scale industrial applications due to perceived limitations in scalability and throughput, often viewed as being confined to laboratory settings. Fortunately, recent advancements in PLD technology have begun to change this perception, bringing innovations such as the development of larger deposition chambers, improved laser sources, and advanced target materials. These improvements have demonstrated that PLD can be effectively scaled up for industrial production, enabling the deposition of high-quality TCO films over larger areas and at higher throughput rates.[7,33–36]

Specifically in PV technologies, AZO has found success in various applications,[37–41] with the record efficiency of 24.94% reached for a SHJ solar cell where the AZO layer was deposited by magnetron sputtering.[42] However, its utilization in perovskite solar cells (PSCs) remains underexplored, with reported efficiencies so far lagging behind those achieved with ITO. Wei et al. and Baltakesmez et al. reported the use of sputtered-AZO films as the bottom electrode of methylammonium lead iodide ($MAPbI_3$) based devices, resulting in efficiencies close to 10%.[43,44] Another report describes a semi-transparent PSC employing sputtered AZO as the top electrode, reaching efficiencies of 16.6%; however, the device stack utilized ITO as the bottom contact, thus still containing indium.[40] Finally, diverging from the conventional TCO usage, sputtered AZO was employed as an electron transport layer in between the perovskite and an ITO bottom electrode, reaching efficiencies of 17.6%.[45]

In this work, we use a scalable PLD method for depositing AZO at room temperature enabling high conductivity, film homogeneity and shelf stability, toward efficient indium-free optoelectronics. First, we investigate the influence of PLD chamber pressure on the optical and electronic characteristics of AZO films composed of 2% aluminum oxide and 98% zinc oxide, using an industrial-grade PLD system. Our findings demonstrate that optimized PLD parameters yield AZO layers with high transmittance (>80% across the visible spectrum) and high conductivity (>1.8×10^5 S m^{-1}). Subsequently, we evaluate the efficacy of these AZO films for preparing opaque and semi-transparent vacuum-processed perovskite solar cells (PSCs) as proof-of-concepts. These devices can achieve power conversion efficiencies comparable or exceeding those of similar devices employing indium-based electrodes. Moreover, we assess the thermal stability of the AZO thin films and solar cells under accelerated aging conditions. Our results emphasize the potential of room temperature PLD-deposited AZO layers as a scalable, viable alternative TCO for next-generation optoelectronic technologies.

2. Results and Discussion

2.1. Pulsed Laser Deposition of AZO

The depositions of the AZO thin films were all carried out at room temperature, i.e., no heating of the substrates nor of the chamber nor of the target. The optimization of the depositions was done with a laser fluence maintained at 1.7–1.8 J cm^{-2} and by adjusting the chamber pressure within a range of 0.010 to 0.050 mbar, regulated by a continuous injection of argon in the PLD chamber. Mixed with argon, a small amount of oxygen was also introduced into the chamber to maintain a constant oxygen partial pressure of 0.002 mbar for all chamber pressures. This ensured a constant exchange of oxygen with the background gas, mitigating alterations in the stoichiometry of ZnO induced by the loss of more-volatile oxygen atoms during the film deposition, thus preventing undesired oxygen vacancies and preserving stoichiometry.

Under lower pressure conditions, utilizing a laser frequency of 50 Hz and with a rectangular laser spot size on the AZO target of 10 mm^2, the growth rate at 0.010 mbar was measured at 200 nm h^{-1}. However, as typical of the PLD deposition, increasing chamber pressure leads to expansion of the plasma plume (see Figure S1 in supporting information), resulting in a reduction in the deposition rate per unit area. Consequently, we observed a threefold decrease in deposition rate as the chamber pressure increased from 0.010 to 0.050 mbar (see Figure S2 in supporting information). Nevertheless, achieving high deposition rates is essential for efficient manufacturing processes. Assuming that increasing the laser frequency and the laser spot area while keeping a similar value of fluence primarily enhances the number of ablated particles without significantly affecting the energy of the ablated species (thus film properties), it is anticipated these laser parameters can be optimized so that the PLD can operate at higher rates. For instance, adjusting the laser frequency to 500 Hz and doubling the laser beam width has the potential to increase deposition rates at low pressures to approximately 4.0 µm per hour. To further evaluate the scalability and homogeneity of the deposition process, an AZO film was deposited over a large circular area of approximately 500 cm^2 (about the size of a 9-inch wafer). Thickness and sheet resistance distribution heatmaps within a square area of approx. 11 × 11 cm^2, concentric with the circular area, are presented in Figure S3 of the Supporting Information. The results indicate that both thickness and sheet resistance are spatially homogeneous, with variations of less than 3.5% across the entire investigated area.

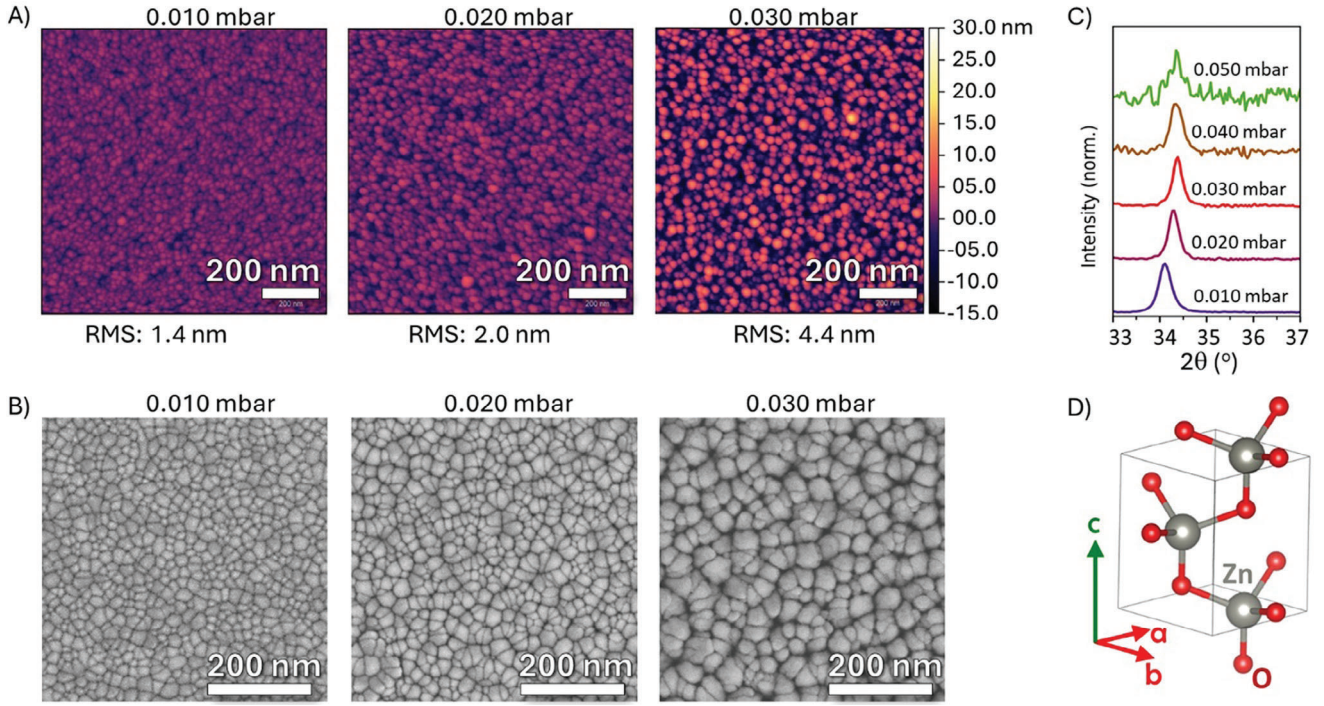

Figure 1. A) AFM surface profiles with RMS roughness values, B) top-view SEM and C) XRD of AZO thin films (110 nm thick) deposited by PLD at different chamber pressures (see full X-ray diffractograms in Figure S5 in the supporting information). D) Zincite crystal structure.

2.2. Characterization of AZO Thin Film

The atomic force microscopy (AFM) analyses shown in **Figure 1**A provides valuable insights into the morphological changes induced by the variations in chamber pressure during PLD deposition. At the lower pressure of 0.010 mbar, a smooth, flat surface was obtained, with a root mean square (RMS) roughness of only 1.4 nm. This suggests a dense, continuous deposition of material, indicative of optimal growth conditions. Films deposited at higher pressures displayed an increasing roughness and porosity, with the emergence of larger voids between the crystal grains followed by an increase in granular structures. This implies a reduction in the material deposition with increasing chamber pressure. Nevertheless, the calculated RMS roughness is still rather low, 4.4 nm. In agreement with AFM findings, scanning electron microscopy (SEM) images also depict a similar evolution of the film morphology with chamber pressure, as observed in Figure 1B and Figure S4 in the supporting information. The deposited AZO thin films predominantly featured columnar crystal structures, presenting a smoother surface when deposited at 0.010 mbar, but with an increased presence of voids between crystals when deposited at a higher pressure. Similar trends between morphology and deposition chamber pressure have also been observed for other oxide thin films deposited by PLD.[35,46,47]

Both energy-dispersive X-ray spectroscopy (EDX) and X-ray photoelectron spectroscopy (XPS) analyses (see the respective spectra in Figures S6 and S7 in the supporting information) highlight slight variations in the Al:ZnO ratio with changing chamber pressures. As summarized in Figure S8 (Supporting Information), across the range of the investigated pressures, the Al content monotonically decreased from 1.7 to 1.1% with increasing chamber pressures as measured by EDX (bulk concentration). A smaller variation was observed by XPS, meaning that the surface composition is virtually unchanged.

To explore the impact of the chamber pressure alterations on the crystallinity of the AZO films, XRD analysis was conducted. Zinc oxide (ZnO, zincite) is known to crystallize in a hexagonal wurtzite structure (space group $P6_3mc$), as shown in Figure 1D. The X-ray diffractograms of the deposited AZO films revealed a main peak around 34.0 to 34.5° (Figure 1C), corresponding to the (002) plane of zincite. This indicates a preferential orientation (or growth) of ZnO along the c-axis, a characteristic commonly observed in PLD-grown ZnO and AZO films,[48,49] and consistent with the columnar growth observed by SEM as discussed above (Figure S4 in the supporting information). Furthermore, as AZO deposition pressures were increased, there was a notable shift in the main signal towards higher angles, indicating a contraction of the lattice along the c-axis at higher deposition pressures. This contraction is most likely not related to differences in the Al content; typically, lattice contraction occurs when there is a greater substitution of larger Zn^{2+} with smaller Al^{3+} ions,[50] which in our AZO films was only observed at lower deposition pressures. Instead, the observed lattice contraction at higher pressures is more likely directly linked to changes in chamber pressure itself rather than variations in Al loading. Although the impact on the crystalline structure is minimal, the levels of Al doping could have significant implications for the optoelectronic properties of the AZO thin films, as will be discussed below.

Conductivity measurements (**Figure 2**A) showed that the AZO thin film deposited at 0.010 mbar exhibited the highest conductivity of 1.8×10^5 S m^{-1} (equivalent to a resistivity of 5.5×10^{-4} Ω.cm, i.e., corresponding to a sheet resistance of ≈55–25 Ω Υ^{-1} for TCO

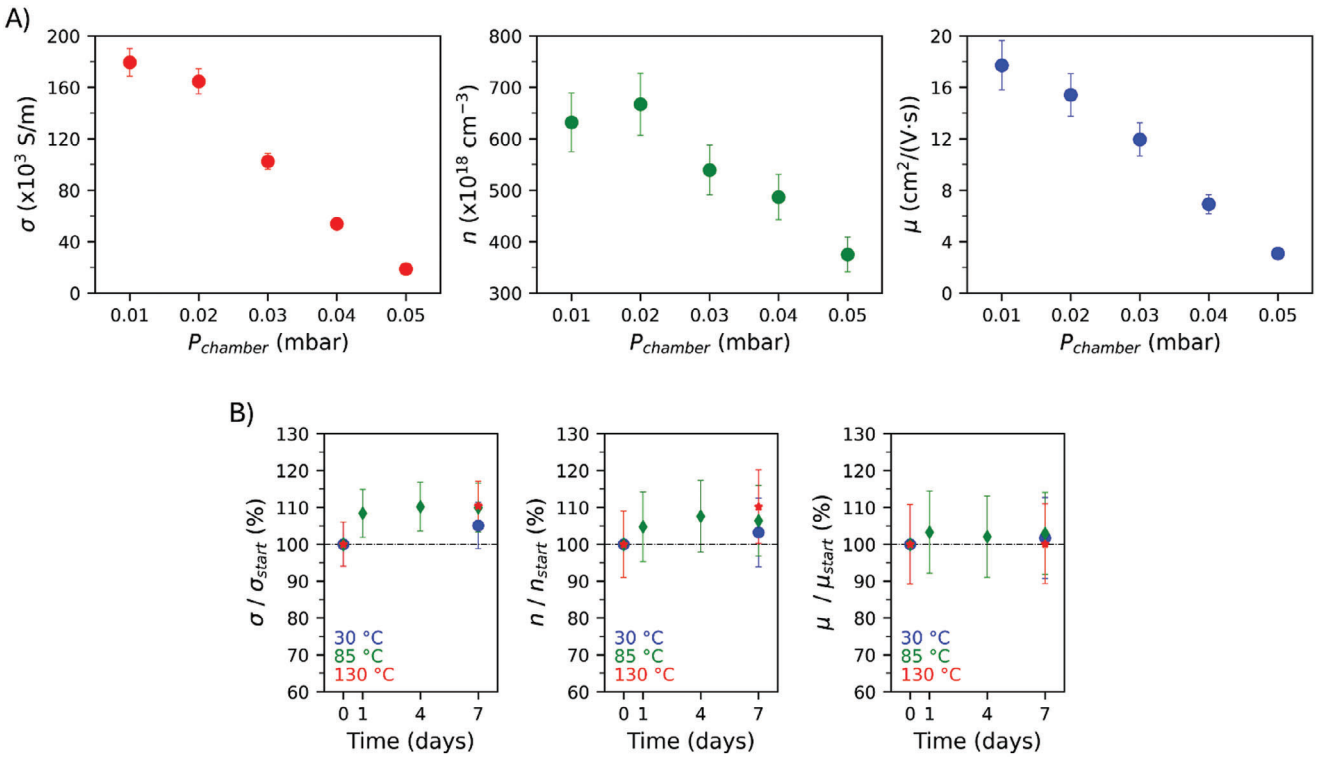

Figure 2. Conductivity (σ), charge carrier concentration (n) and mobility (μ) of AZO thin films. A) electric properties versus different deposition chamber pressures; B) electric properties of samples deposited at 0.010 mbar versus time of exposure to air (relative humidity between 60–80%) at 30 °C, 85 °C or 130 °C.

thicknesses typically seen in PSCs, around 100 to 200 nm). It's noteworthy that such a room-temperature process like our PLD method can achieve such a remarkable conductivity, yielding one of the lowest resistivities for any AZO thin films thinner than 700 nm, comparable to or even lower than the ones obtained by more conventional deposition methods that require higher temperatures and harsher conditions.[29] In fact, as reviewed by Moralis-Masis et al.,[2] our PLD-AZO films rank among the top-performing TCOs in terms of conductivity, outperformed only by indium-based materials or those deposited at very high temperatures, some exceeding 400 °C.

The conductivity (σ) increased almost linearly with decreasing chamber pressures. Hall effect measurements indicate that the enhanced conductivity obtained for the film deposited at 0.010 mbar is the result of a combination of a higher charge carrier concentration (η, measured as 6.5×10^{20} cm^{-3}) resulting from higher levels of Al doping, and a larger charge mobility (μ, measured as 18 cm^2 V^{-1} s^{-1}) facilitated by the more-compact film morphology. Since an increase in chamber pressure results in lower Al concentration (reduced doping level) and increased roughness, the corresponding AZO films exhibited lower charge carrier concentration and mobility.

To evaluate the shelf-stability of the AZO films, a sample deposited at 0.010 mbar was left exposed to air for one week either without or with heating at 85 and 130 °C. Subsequently, its electrical properties were measured (as depicted in Figure 2B), revealing no significant changes in conductivity, mobility, or charge carrier concentration. This observation suggests that the films exhibit good stability not only under typical storage conditions but also under thermal stressing, which is crucial for their practical application in various optoelectronic devices. Additionally, the electric parameters of an AZO film deposited at 0.010 mbar all improved when the film was subjected to post-annealing in N_2 atmosphere (Figure S9 in the Supporting Information).

The glass/AZO substrates also have remarkable optical properties, with transmittance surpassing 80% and absorptance below 10% across the visible spectrum, irrespective of the deposition pressure, as depicted in **Figure 3**A,B. Notable in Figure 3C, the extinction coefficient within the wavelength range of 400 to 1000 nm approached zero, a highly advantageous feature for TCO's applied in PSCs as it minimizes parasitic absorption from the TCO. Therefore, our PLD-AZO films deposited at room temperature exhibit not only high conductivity but also exceptional transparency, making them ideal for use as TCOs in solar cells. Beyond 1150 nm, however, near-infrared (NIR) radiation interacts with free electrons in the conduction band, increasing the extinction coefficient. Interference phenomena lead to the observation of reflectance fringes in the visible spectrum, as depicted in Figure 3D. Slight discrepancies were observed in the reflectance of AZO films deposited across various chamber pressures, mainly arising from small differences in their targeted thickness (≈110 nm), but also from different refractive indices, as illustrated in Figure 3E. Notably, AZO samples deposited at lower pressures exhibited lower refractive indices, a finding consistent with previous reports due to their higher charge carrier

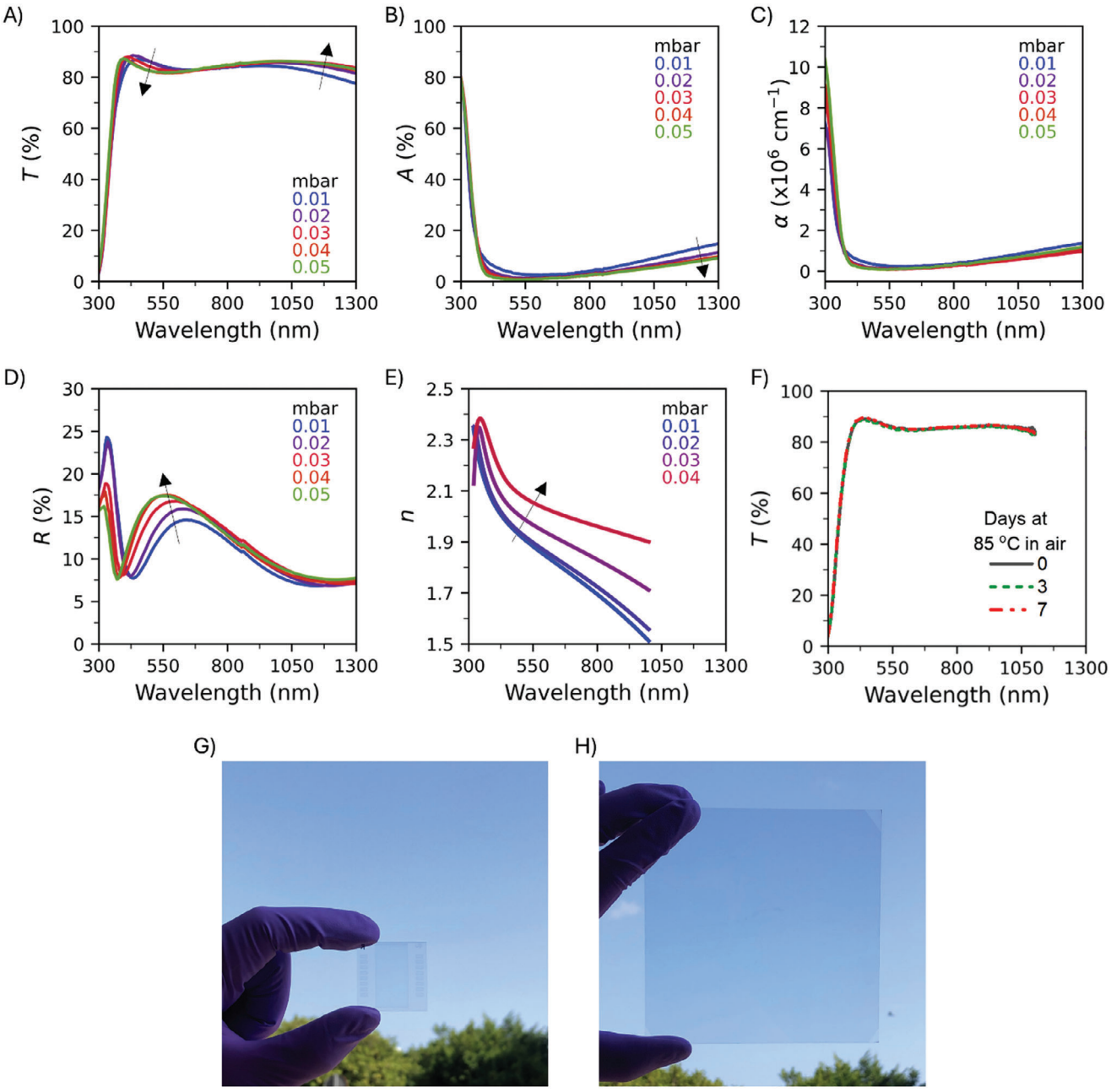

Figure 3. A) Transmittance, B) absorptance, C) extinction coefficient, D) reflectance and E) refractive index of AZO thin films (≈110 nm) deposited on glass by PLD under different chamber pressures (blank: air); the arrows were placed for easier observation of the trend with increasing chamber pressures. F) Transmittance spectra of an AZO thin film deposited at 0.010 mbar versus time of exposure to air at 85 °C, showing no changes after 7 days of stressing. G and H) Pictures of the light being transmitted through AZO thin films (≈120 nm) deposited on glass substrates with different sizes (either 3×3 or 12×12 cm^2).

concentration.[51–55] Prolonged (7 days) exposure of an AZO film deposited at 0.010 mbar to air at 85 °C did not lead to any changes in the transmittance spectrum (Figure 3F), indicative of the good shelf stability of these PLD AZO films.

The images in Figure 3G,H demonstrate that the AZO films exhibit smooth, even surfaces without any visible patterns or textures. Light is transmitted uniformly across the entire glass/AZO substrates, whether on smaller 3×3 cm^2 substrates with patterned deposition or larger 12×12 cm^2 substrates. The final product resembles a neutral density filter, darkening the scene uniformly behind it.

Therefore, the AZO thin films showed excellent conductivity, transmittance, and stability, which may be attributed to key advantages intrinsic to PLD. PLD provides precise stoichiometric control, critical for maintaining the optimal Al ratio that directly affects the performance of AZO films, and its high-energy

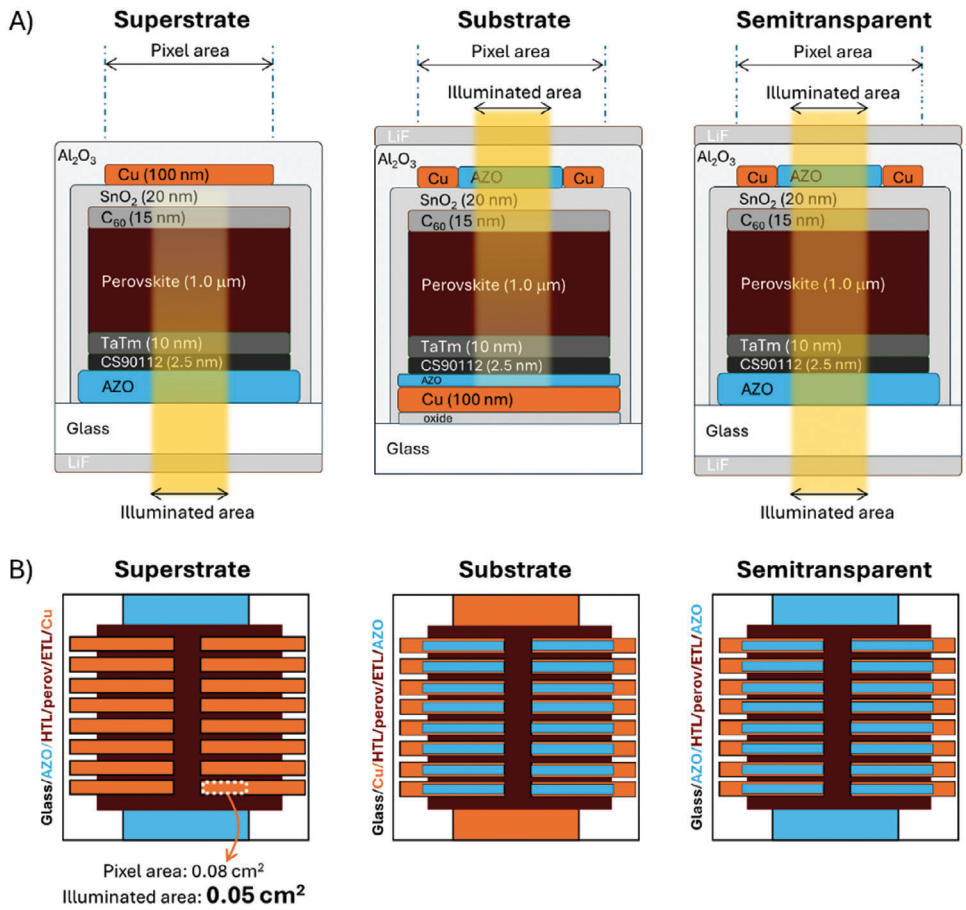

Figure 4. Device configurations employed: superstrate, substrate, or semitransparent. Cross-sectional representation not drawn to scale.

deposition promotes better crystallinity and denser films with fewer defects, enhancing both conductivity and stability.

2.3. Use of AZO Thin Films in PSCs

To further demonstrate the applicability of the PLD-deposited AZO films as a replacement for ITO in optoelectronic devices, they were integrated into p-i-n PSCs as proof-of-concept using three distinct device configurations, as depicted in **Figure 4**. In all these device configurations, the layer sequence consisted of glass/bottom electrode/CS90112 (2.5 nm)/TaTm (10 nm)/$MAPbI_3$ (1000 nm)/C_{60} (15 nm)/SnO_2 (20 nm)/top-electrode. Here, CS90112 is 2,2′,2″-(cyclopropane-1,2,3-triylidene)tris(2-(p-cyanotetrafluorophenyl)-acetonitrile, TaTm is N4,N4,N4″,N4″-tetra([1,1′-biphenyl]−4-yl)-[1,1′:4′,1″-terphenyl]−4,4″-diamine, and C_{60} is fullerene. We employed the archetype methyl ammonium lead triiodide as the perovskite that was sublimed by co-sublimation of the methylammonium iodide and lead iodide precursors to a thickness of 1 micrometer using the procedure described previously by us (details can be found in the experimental section).[56,57] In this stack, the SnO_2 film was deposited by atomic layer deposition (ALD), functioning not only as an electron transport layer but also as a barrier coating preventing exposure of the stack to air which leads to a higher stability. Furthermore, a compact layer of Al_2O_3 was deposited by ALD, providing an additional encapsulation layer for the entire device, followed by the deposition of LiF on top to serve as an anti-reflective coating. In the "superstrate" configuration, AZO films served as the bottom-electrode deposited directly onto glass, while metallic Cu films were used as the top contacts. These devices are characterized by illumination through the bottom glass side. On the other hand, the "substrate" layout is optimized for top illumination, featuring a thin Cu layer as the bottom electrode on glass, with AZO layers deposited as transparent top-electrodes. In the substrate layout, a thin layer of MoO_3 was thermally evaporated in between the glass and the Cu electrode to ensure adhesion of the metal to the glass,[58] and a thin layer of AZO was deposited on top of the Cu electrode to ensure a consistent surface morphology through all the three device configurations. In the semitransparent arrangement, both bottom and top electrodes consist of AZO layers. Regardless of their architecture, each device contains sixteen active cells.

Optimization of these solar cells started by identifying the ideal thicknesses for both the AZO layer and the LiF antireflective coating to maximize the photogenerated current. To achieve this, we used optical simulations based on transfer matrix calculations to determine the absorptance and 1-reflectance (1-R) spectrum of the device stack as a function of AZO and LiF thicknesses. The computations took into account the optical properties of the

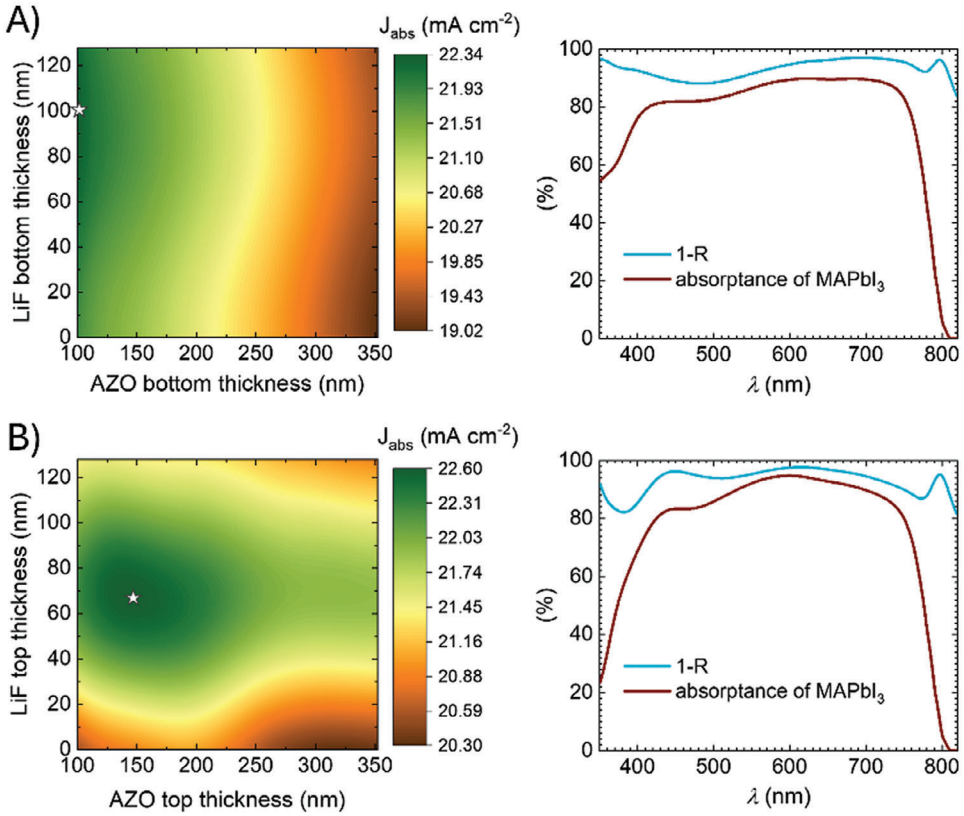

Figure 5. Contour plots of simulated J_{abs} values (in mA cm^{-2}) as a function of LiF and AZO thicknesses as well as simulated abs and 1-R spectra of AZO-based semitransparent cells when illuminated from bottom A) or top B). The stars in the contour plots represent the point with the thicknesses that should lead to the highest J_{abs}. The abs and 1-R spectra shown correspond to the simulated spectra of the point represented with a star.

most-conductive AZO film deposited at 0.010 mbar and with a minimum threshold thickness of 100 nm. Thinner films were not simulated due to the likelihood of incurring series resistance losses owing to higher sheet resistances. The simulated absorptance and 1-R spectra obtained should respectively correlate to the external and internal quantum yields of the fabricated devices. Then, the absorptance spectra were integrated over the AM 1.5 G irradiance and processed mathematically to derive equivalent current densities, J_{abs}, with the contour plots illustrated in **Figure 5**. The optimal thicknesses of AZO and LiF for both bottom and top AZO electrodes were identified by locating the regions in the contour plots where the values of J_{abs} were maximized. For the bottom electrode, they were found to be approximately 100 nm of AZO with 100 nm of LiF, while for the top electrode, 145 nm of AZO with 75 nm of LiF was identified as the best configuration.

Having determined the optimized thicknesses of AZO and LiF for both bottom and top electrodes, we proceeded to fabricate devices in all three configurations depicted in Figure 4. Their performances were evaluated by measuring their current density – voltage (JV) curves under AM 1.5 G irradiance, their external quantum efficiency (EQE) spectra and maximum power point (MPP) tracking, as illustrated in **Figure 6**A–C. A summary of their performance is provided in Figure 6D as well as in **Table 1**, and their dark JV curves are exhibited in Figure S12 in the supporting information.

The superstrate devices reached a power conversion efficiency (PCE) of 18.5% when 100 nm of AZO deposited at 0.010 mbar was as the bottom electrode, but only 17.0% when the employed AZO was deposited at 0.020 mbar, caused by a decrease in the FF. This decrease in FF is in agreement with the increased sheet resistance of the AZO layers deposited at that chamber pressure. The short-circuit current density (J_{sc}) for the two superstrate devices were quite similar, around 22.7 mA cm^{-2}, which is expected in view of the similar absorption of the two AZO films. The open-circuit voltage (V_{oc}) obtained for samples with bottom AZO deposited at 0.020 mbar reached 1.085 V, almost 15 mV higher than for the device employing the AZO layer deposited at 0.010 mbar. It is noteworthy that the EQE spectrum of this sample closely resembled the simulated absorptance spectrum depicted in Figure 5, thereby confirming the validity of the conducted simulations and the high quality of the perovskite absorber.

Similarly, to check the best deposition conditions for AZO to be used as top contacts, a subset of semitransparent devices was fabricated with different AZO top contacts deposited at varying chamber pressures. For these semitransparent devices we employed an AZO bottom electrode deposited at 0.010 mbar in view of the results obtained for the opaque cells as described above. The top AZO electrodes used were deposited using three different chamber pressures, namely at 0.010, 0.020, and 0.030 mbar, with a targeted thickness of 145 nm. These semitransparent

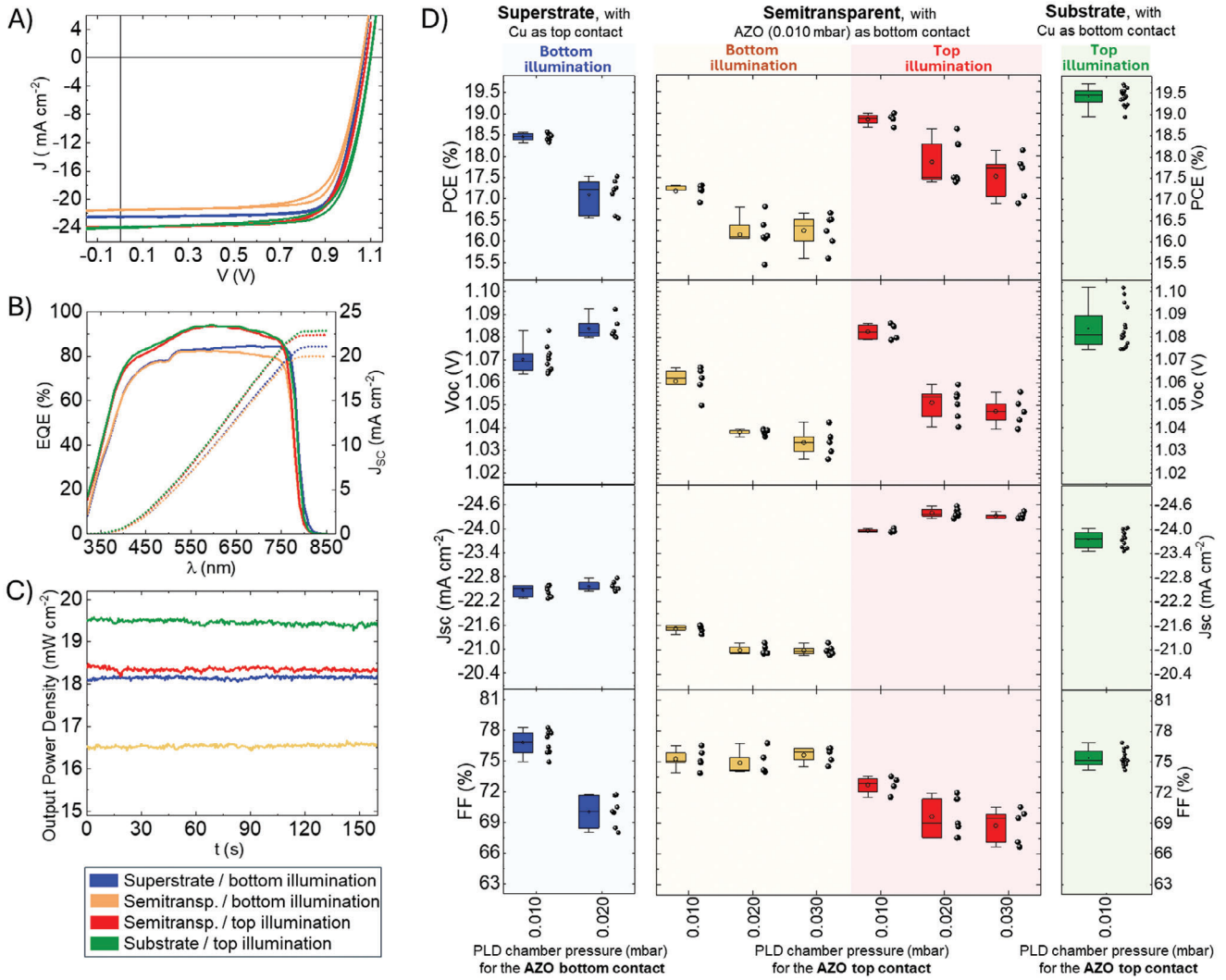

Figure 6. A) Illuminated JV curves (forward and reverse scans) and B) EQE spectra of the best cells of the superstrate, semitransparent and substrate devices using AZO deposited at 0.010 mbar as bottom- and/or top-electrodes. C) Maximum power point tracking of a randomly selected sample of a superstrate, semitransparent and substrate devices using AZO deposited at 0.010 mbar as bottom- and/or top-electrodes. D) Statistic distribution of the photovoltaic performance of superstrate, semitransparent and substrate devices using AZO as bottom and/or top-electrodes deposited under different PLD chamber pressures (sample size: 8 to 16 devices). Samples were measured in air under AM 1.5 G irradiation (0.05 cm^2) at 100 mW cm^{-2} at room temperature.

Table 1. Average photovoltaic performance of superstrate, substrate and semitransparent devices using AZO deposited by PLD at 0.010 mbar as bottom- and/or top-electrodes. A standard device fabricated swapping AZO for ITO is shown for comparisons. Samples were measured in air under AM 1.5 G irradiation (0.05 cm^2) at 100 mW cm^{-2} at room temperature. Sample size: 8 to 16 samples.

		Series resistance [Ω cm^{-2}]	V_{oc} [V]	J_{sc} [mA cm^{-2}]	FF [%]	PCE [%]
AZO	Superstrate (bottom illumination)	5.2	1.070 ± 0.005	22.5 ± 0.1	76.8 ± 1.1	18.5 ± 0.1
	Semitransparent (bottom illumination)	5.1	1.060 ± 0.006	21.5 ± 0.1	75.3 ± 1.3	17.2 ± 0.2
	Semitransparent (top illumination)	6.8	1.082 ± 0.004	24.0 ± 0.1	72.7 ± 0.9	18.9 ± 0.1
	Substrate (top illumination)	2.5	1.083 ± 0.009	23.8 ± 0.2	75.4 ± 0.8	19.4 ± 0.2
ITO	Superstrate (bottom illumination)	2.0	1.073 ± 0.006	21.9 ± 0.1	78.8 ± 0.9	18.5 ± 0.1
	Semitransparent (bottom illumination)	5.6	1.094 ± 0.004	21.3 ± 0.2	76.4 ± 0.9	17.6 ± 0.3
	Semitransparent (top illumination)	4.3	1.093 ± 0.004	23.4 ± 0.2	74.9 ± 0.8	19.0 ± 0.2

devices were evaluated by illumination from either the bottom or the top side. When illuminated through the bottom contact a lower Jsc was obtained in comparison with the opaque cells. This is due to the reduced optical path length in the semitransparent devices due to the absence of a reflective top electrode. From the EQE (Figure 6) it can be observed that this loss is mostly originating for wavelengths above 700 nm. However, when these semitransparent devices were illuminated from the top side, the J_{sc} was significantly higher than what was obtained for the opaque cells (>24 versus 22 mA cm^{-2}, respectively). This is a result of an almost ideal anti-reflection stack air/LiF/Al_2O_3/AZO which led to a significant increase in light entering into the device.[59] Consequently, the EQE of the semitransparent device reached values as high as 95% under top illumination. J_{sc} values exceeding 24.0 mA cm^{-2} is a noteworthy milestone for solar cells made with co-evaporated-$MAPbI_3$. The resemblance between the EQE spectrum of this sample and the simulated absorptance spectrum illustrated in Figure 5 is remarkable. The higher light absorption for top illumination also led to higher V_{oc} values, which might be related to the higher carrier concentration. The FF of semitransparent devices illuminated through the bottom AZO electrode did not vary much for the three different devices (the top AZO deposited at the chamber pressure of 0.010, 0.020, and 0.030 mbar). The FF value was very close to that of the opaque device with the same AZO bottom electrode. On the other hand, when these semitransparent devices were evaluated by illuminating through the top AZO electrode, the FF decreased for the devices containing more-resistant AZO top electrodes deposited at higher chamber pressures. This implies that the higher current density generated from the top illumination exacerbates the adverse effects caused by series resistances: these resistances create additional voltage drops along the path of the current, impacting FF and overall device efficiency. To reduce the series resistance for the top AZO metal grid lines were deposited outside the active area of the cells. We demonstrated the benefit of such grid lines in our previously published ITO top electrode PSCs.[35] Overall, the best performing semitransparent devices were obtained under top illumination and employing a top AZO electrode deposited at 0.010 mbar, reaching a PCE of 18.9%.

Finally, we also prepared devices in the substrate configuration employing a metallic bottom electrode (100 nm of Cu covered with a thin layer of AZO deposited at 0.010 mbar) and a 145 nm thick AZO top electrode deposited at 0.010 mbar. Substrate configuration devices also benefit from the almost ideal anti-reflection stack used in the semitransparent devices. Thus, the EQE and J_{sc} (≈24 mA cm^2) for the substrate devices were similar to those achieved by top illuminating the semitransparent devices. This suggests that the reflecting bottom electrode has a negligible effect on increasing the optical path length, and that nearly all sunlight with energy above the absorber bandgap is absorbed by the 1-micrometer $MAPbI_3$ film. The Cu bottom contact led to improved rectification in both dark and illuminated JV curves, which resulted in slightly higher FF as compared to the semitransparent device, which led to a PCE value of 19.4%. These results are among the best for $MAPbI_3$ based evaporated solar cells and thus qualify the PLD deposited AZO electrode as a suitable alternative for indium containing TCOs.

In parallel, for comparison, we prepared superstrate and semitransparent devices with identical thin film stacks as the investigated AZO-based devices but utilizing ITO for both bottom and/or top contacts. These standard ITO devices had 150 nm and/or 140 nm of ITO in the bottom- and/or top-contacts, respectively, as optimized in another publication.[60] Their photovoltaic characteristics summarized in Table 1, obtained form the JV curves presented in Figure S13 in the supporting information. The performance achieved for ITO-based devices was equivalent to that of PSCs with PLD-AZO in all the investigated configurations. This confirms that AZO is a suitable TCO and can replace ITO.

Finaly, to assess the long-term stability of the fabricated solar cells, both superstrate and semitransparent devices containing AZO TCO were heated at 85 °C in a N_2 glove box. **Figure 7** shows the evolution of the photovoltaic parameters of the devices stressed at 85 °C monitored at specified intervals. Both the semitransparent and the superstrate cells retained 80% of their initial efficiency ($t_{80\%}$) for approximately 1800 hours (75 days) under continuous heating. For all samples, it is noteworthy that the J_{sc} and V_{oc} remained practically constant throughout the experiment duration. For both superstrate and semitransparent devices, the only factor contributing to the decrease in PCE was a gradual loss in FF. This decrease in FF is the result of increased series resistances over time as observed from their JV curves in Figure 7B. Given that the PLD-AZO thin films had not exhibited alterations in conductivity and transmittance under heat stressing as discussed above, the increased series resistance losses in the stressed devices indicate that the charge extraction is affected over time. Since in our pin devices we employed a thin interface layer of CS90112 in combination with the TaTm HTL, this decrease in charge extraction is most likely caused at that interface. The ITO-based devices also experienced a similar decrease in FF after thermal stressing, suggesting that the drop in FF is inherent to our chosen device stack, regardless of the employed TCO. In fact, the stability of these devices made with ITO are comparable to the ones with AZO, also expected to take ≈1800 hours to reach 80% of the initial efficiency, as shown in Figure S14 in the supporting information.

3. Conclusion

Room temperature pulsed laser-deposited AZO films exhibit exceptional properties, such as optical transparency (> 80% over 400 to 1000 nm) and high conductivity (1.8×10^5 S m^{-1}), standing as one of the lowest resistivities observed for AZO films obtained at room temperature. Importantly, their optical and electrical properties are maintained even under prolonged exposure to elevated temperatures and air/moisture, demonstrating their reliability in harsh environmental conditions. To showcase their versatility, the AZO films were employed as transparent electrodes in indium-free perovskite solar cells, notably exploring their application as a top contact in addition to their conventional use as a bottom contact. Three different configurations were successfully fabricated, achieving power conversion efficiencies exceeding 18.5% and 19.4% in superstrate and substrate configurations, respectively, while semi-transparent solar cells reached PCEs up to 19.0%. These performances are on par with state-of-the-art solar cells using indium-based TCOs. These solar cells employing PLD AZO electrodes exhibit long thermal stability, with $t_{80\%}$ higher than 1800 hours at 85 °C.

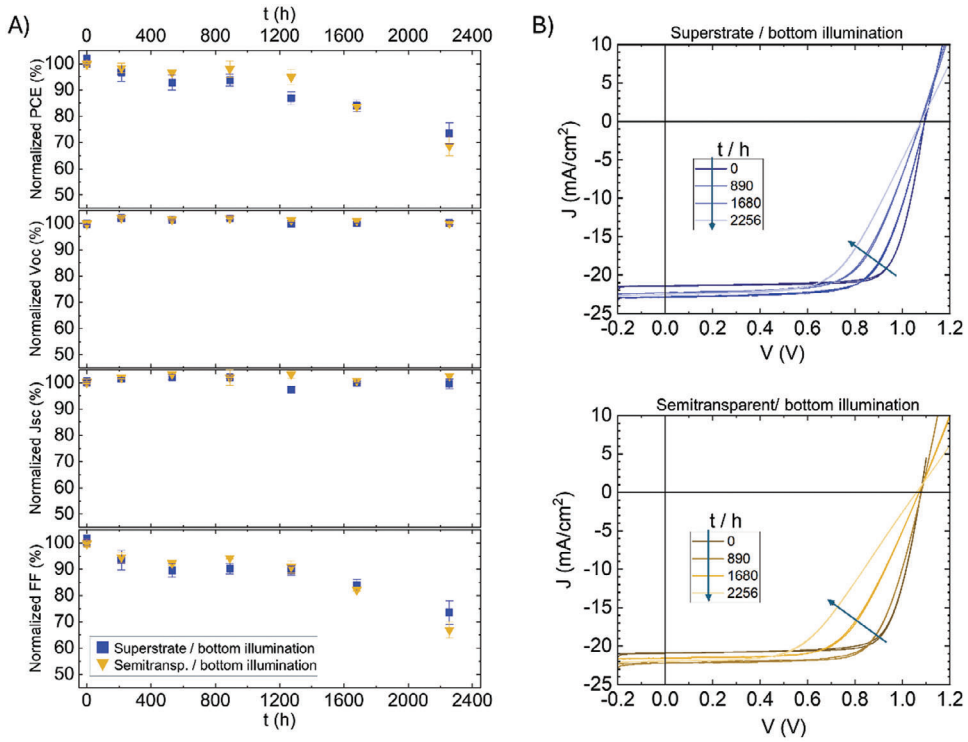

Figure 7. A) Evaluation of the photovoltaic parameters (average and standard deviation) and B) JV curves of AZO-based PSCs in the superstrate or semitransparent configurations as a function of aging time in nitrogen atmosphere at 85 °C (in dark). Samples were measured in air under AM 1.5 G irradiation (0.05 cm^2) at 100 mW cm^{-2} at room temperature. Sample size: 8 samples.

Our findings demonstrate that PLD-deposited AZO layers can advance optoelectronic technologies as a sustainable alternative to indium based TCO's, offering scalability and versatility to innovative device manufacturing.

4. Experimental Section

Industrial Scale PLD System: The AZO films were deposited on glass substrates and directly on the top-layers of PSCs at room temperature using a Solmates large area PLD 200 mm system. The AZO was deposited through shadow masks to ensure fixed electrode areas. The system was equipped with a droplet trap to reduce the number of undesired particles on the deposited film, which allows for a homogeneous deposition on large areas. This PLD tool was coupled to a N_2 glovebox, to minimize any detrimental effects from O_2 and moisture on the performance of the finally produced devices. A Lightmachinery's IPEX-700 KrF excimer laser (λ = 248 nm) was employed, setting the repetition rate at 50 Hz and a fluence of 1.7–1.8 J cm^{-2}. The source material for AZO deposition was a Al:ZnO ceramic target with 2:98 wt.%, acquired from Pi-kem.

Optical Simulation: Transfer matrix method-based absorptance and 1-R simulations were performed in a home-built code that uses the tmm package on a python-based IDE. The derivations of the formulas and calculations implemented to develop the tmm package were published elsewhere.[61] The optical constants used in the simulations of all the layers of the stack were shown in Figure S15 in the supporting information. A Sentech Senpro4 ellipsometer was used to extract refractive indices and absorption coefficients.

Device Fabrication: All the solar cell layers were prepared by thermal vacuum deposition performed in vacuum chambers evacuated to a pressure of 10^{-6} mbar, which were integrated into a nitrogen-filled glovebox (O_2 and H_2O below 1 ppm). In general, the vacuum chambers were equipped with temperature-controlled evaporation sources (Creaphys) fitted with ceramic crucibles. The sources were directed upward with an angle of ≈90° with respect to the bottom of the evaporator. The distance between the substrate holder and the evaporation source was approximately 20 cm. Individual quartz crystal microbalance (QCM) sensors monitored the deposition rate of each evaporation source and another one close to the substrate holder monitored the total deposition rate.

PLD-deposited AZO on glass was used as the substrate for superstrate or semitransparent devices; devices with substrate configuration had glass/MoO_3 (5nm)/Cu (100 nm)/AZO (40 nm) as a substrate,[58] deposited by thermal vacuum using a deposition chamber integrated in an inert N_2 filled glovebox (O_2 and H_2O below 1 ppm) deposition as recently described, with the same pattern as the glass/AZO substrates. For the perovskite deposition, MAI and PbI_2 were coevaporated at the same time by measuring the deposition rate of each material in two QCM sensors and obtaining the total perovskite thickness in a third one located closer to the substrates, as recently described by us elsewhere,[56,57] leading to a final thickness of 1 µm. CS90112, TaTm, and C_{60} were sublimed in a dedicated deposition chamber integrated in an inert N_2 filled glovebox (O_2 and H_2O below 1 ppm) with temperatures around 190, 320, and 390 °C, respectively; in general, the deposition rates were 0.3–0.5 Å s^{-1}. SnO_2 was deposited by ALD following a procedure published by us elsewhere[36] using an Arradiance's GEMStar XT Thermal ALD system integrated into a nitrogen-filled glovebox. MoO_3, Ag and LiF were evaporated in a third deposition chamber integrated in an inert N_2 filled glovebox (O_2 and H_2O below 1 ppm) using aluminum boats as sources by applying currents ranging from 2.0 to 4.5 A. The devices were encapsulated using ALD of Al_2O_3 at 40 °C, using a protocol published by us elsewhere.[62]

Thin Film Characterization: AFM measurements of the sample surfaces were performed obtained using a Bruker ICON Dimension microscope in tapping mode. SEM images were taken with a High Resolution Field Emission Scanning Electron Microscope (HR-FESEM) Zeiss GenimiSEM 500 model, with a secondary Electron In-Lens detector using an accelerating voltage of 1 kV. The EDX images were taken with the same

equipment provided with a X-Ray Dispersive Energy Detector (Oxford Instrument). XPS spectra were recorded using a Thermo Scientific KAlpha with a monochromatic Al Kα X-ray source (1486.6 eV); data were analyzed and deconvoluted with Avantage software, and the binding energies were adjusted to the standard C 1s peak at 284.6 eV. Thicknesses were measured with an Ambios XP1 mechanical profilometer. X-ray diffraction patterns were measured with a Panalytical Empyrean diffractometer equipped with a Cu Kα anode operated at 45 kV and 30 mA and a Pixel 1D detector in scanning line mode; single scans were acquired in the $2\theta = 10°–60°$ range in Bragg–Brentano geometry in air. The conductivity, charge carrier concentration and mobility of the AZO films were measured at room temperature (30 °C) and at a working pressure below 8×10^{-4} mbar using a thin film analyzer (TFA) from Linseis. The working principle of these measurements was based on the Hall effect and was described elsewhere.[63] The errors in the obtained values were governed by the repeatability and accuracy of the measurements and equipment, and were given for every measurement (i.e., $\pm$ 6% for σ, $\pm$ 9% for n and $\pm$ 10.8% for μ). The reflectance and transmittance spectra were measured using a PerkinElmer Lambda 950 UV–vis- NIR spectrometer coupled with an integrating sphere. The absorptance spectra were determined based on the premise that the sum of reflectance, transmittance, and absorptance equals one.

Device Characterization: The JV curves for the solar cells were recorded using a Keithley 2612A SourceMeter in −0.2 and 1.2 V voltage range with 0.01 V steps and integrating the signal for 20 ms after a 10 ms delay, corresponding to a speed of about 0.3 V s^{-1}. The devices were illuminated under a Wavelabs Sinus 70 AAA LED solar simulator. Before each measurement, the illumination intensity was calibrated to 1 sun using a calibrated silicon reference diode with an infrared cutoff filter (KG-5, Schott). The mismatch factor was calculated to be 1.011 by comparing the spectral irradiance of the AM 1.5G solar spectrum and the LED simulator against the external quantum efficiency (EQE) of both the reference silicon cell and the $MAPbI_3$ solar cell.[59] Devices had a total area of 0.083 cm^2 and an illuminated area of 0.050 cm^2, defined through the use of metal shadow masks during the deposition and measurement process. During experiments, the encapsulated devices were exposed to air, and the temperature was stabilized at 298 K using a cooling system controlled by a Peltier element. External quantum efficiency (EQE) was measured using a QE-R system developed by Enli Technology Co., Ltd.

Supporting Information

Supporting Information is available from the Wiley Online Library or from the author.

Acknowledgements

The authors acknowledge financial support of the European Research Council (ERC) under the European Union's Horizon 2020 research and innovation programme (Grant Agreement No. 834431). Funded by the European Union; views and opinions expressed were however those of the authors only and do not necessarily reflect those of the European Union or CINEA; neither the European Union nor the granting authority can be held responsible for them. VALHALLA project has received funding from Horizon Europe Research and Innovation Action programme under Grant Agreement n° 101082176. Authors acknowledge support from the Comunitat Valenciana (MFA/2022/022, CISEJI/2022/43, IDI-FEDER/2021/078). Authors also acknowledge support from the Ministry of Science and Innovation (MCIN) and the Spanish State Research Agency (AEI): project TED2021-129679B-C21 and grant IJC2020-045130-I funded by MCIN/AEI/10.13039/501100011033 and by the "European Union NextGenerationEU/PRTR"; grant RYC2019-027187 funded by MCIN/AEI/10.13039/501100011033 and by "ESF investing in your future"; project CEX2019-000919-M funded by MCIN/AEI/10.13039/501100011033; project PCI2023-145969-2 funded by MICIU/AEI /10.13039/501100011033 and co-funded by the European Union.

Conflict of Interest

The authors declare no conflict of interest.

Data Availability Statement

The data that support the findings of this study are openly available in [Zenodo] at [https://doi.orsig/10.5281/zenodo.13470801], reference number [13470801].

Keywords

aluminum-doped zinc oxide, perovskite solar cell, pulsed-laser deposition, transparent conductive oxide

Received: September 25, 2024
Revised: November 4, 2024
Published online:

[1] H. Liu, V. Avrutin, N. Izyumskaya, Ü. Özgür, H. Morkoç, *Superlattices Microstruct.* **2010**, *48*, 458.
[2] M. Morales-Masis, S. De Wolf, R. Woods-Robinson, J. W. Ager, C. Ballif, *Adv. Electron. Mater.* **2017**, *3*, 1600529.
[3] T. Minami, *Semicond. Sci. Technol.* **2005**, *20*, S35.
[4] S. De Wolf, A. Descoeudres, Z. C. Holman, C. Ballif, *Green.* **2012**, *2*, 7.
[5] J. Haschke, R. Lemerle, B. Aissa, A. A. Abdallah, M. M. Kivambe, M. Boccard, C. Ballif, *IEEE J. Photovolt.* **2019**, *9*, 1202.
[6] E. Aydin, C. Altinkaya, Y. Smirnov, M. A. Yaqin, K. P. S. Zanoni, A. Paliwal, Y. Firdaus, T. G. Allen, T. D. Anthopoulos, H. J. Bolink, M. Morales-Masis, S. De Wolf, *Matter.* **2021**, *4*, 3549.
[7] Y. Smirnov, L. Schmengler, R. Kuik, P. Repecaud, M. Najafi, D. Zhang, M. Theelen, E. Aydin, S. Veenstra, S. De Wolf, M. Morales-Masis, *Adv. Mater. Technol.* **2021**, *6*, 2000856.
[8] J. Zhang, X. Hu, H. Li, K. Ji, B. Li, X. Liu, Y. Xiang, P. Hou, C. Liu, Z. Wu, Y. Shen, S. D. Stranks, S. R. P. Silva, H. Cheng, W. Zhang, *Adv. Funct. Mater.* **2021**, *31*, 2104396.
[9] D. Li, D. Zhang, K. Lim, Y. Hu, Y. Rong, A. Mei, N. Park, H. Han, *Adv. Funct. Mater.* **2021**, *31*, 2008621.
[10] N.-G. Park, K. Zhu, *Nat. Rev. Mater.* **2020**, *5*, 333.
[11] M. Kim, Y. Zhang, P. Verlinden, B. Hallam, *AIP Conf. Proc.* **2022**, *2487*, 090001.
[12] M. Gómez, G. Xu, J. Li, X. Zeng, *Environ. Sci. Technol.* **2023**, *57*, 2611.
[13] C. Bright, presented at *51st Annual Technical Conference Proceedings*, Chicago, IL, **2008**, pp. 840–850.
[14] M. Lokanc, R. Eggert, M. Redlinger, *The Availability of Indium: The Present, Medium Term, and Long Term*, Golden, CO (US) **2015**, https://www.nrel.gov/docs/fy16osti/62409.pdf.
[15] E. Ching-Prado, A. Watson, H. Miranda, *J. Mater. Sci. Mater. Electron.* **2018**, *29*, 15299.
[16] R. Ramarajan, D. Paul Joseph, K. Thangaraju, M. Kovendhan, *Cham.* **2021**, *55*, 149.
[17] J. Troughton, D. Bryant, K. Wojciechowski, M. J. Carnie, H. Snaith, D. A. Worsley, T. M. Watson, *J. Mater. Chem. A.* **2015**, *3*, 9141.
[18] F. Qin, J. Tong, R. Ge, B. Luo, F. Jiang, T. Liu, Y. Jiang, Z. Xu, L. Mao, W. Meng, S. Xiong, Z. Li, L. Li, Y. Zhou, *J. Mater. Chem. A.* **2016**, *4*, 14017.
[19] B. T. Feleki, S. Chandrashekar, R. K. M. Bouwer, M. M. Wienk, R. A. J. Janssen, *Sol. RRL.* **2020**, *4*, 2000385.
[20] B. T. Feleki, R. K. M. Bouwer, V. Zardetto, M. M. Wienk, R. A. J. Janssen, *ACS Appl. Energy Mater.* **2022**, *5*, 6709.

[21] J. Werner, C. C. Boyd, T. Moot, E. J. Wolf, R. M. France, S. A. Johnson, M. F. A. M. van Hest, J. M. Luther, K. Zhu, J. J. Berry, M. D. McGehee, *Energy Environ. Sci.* **2020**, *13*, 3393.
[22] J. Zhang, X.-G. Hu, K. Ji, S. Zhao, D. Liu, B. Li, P.-X. Hou, C. Liu, L. Liu, S. D. Stranks, H.-M. Cheng, S. R. P. Silva, W. Zhang, *Nat. Commun.* **2024**, *15*, 2245.
[23] H. Guo, F. Hou, X. Ren, X. Ning, Y. Wang, H. Yang, J. Wei, J. Guo, T. Li, C. Zhu, Y. Zhao, X. Zhang, *Sol. RRL.* **2023**, *7*, 2300333.
[24] A. Harter, S. Mariotti, L. Korte, R. Schlatmann, S. Albrecht, B. Stannowski, *Prog. Photovoltaics Res. Appl.* **2023**, *31*, 813.
[25] F. Yang, P. Tockhorn, A. Musiienko, F. Lang, D. Menzel, R. Macqueen, E. Köhnen, K. Xu, S. Mariotti, D. Mantione, L. Merten, A. Hinderhofer, B. Li, D. R. Wargulski, S. P. Harvey, J. Zhang, F. Scheler, S. Berwig, M. Roß, J. Thiesbrummel, A. Al-Ashouri, K. O. Brinkmann, T. Riedl, F. Schreiber, D. Abou-Ras, H. Snaith, D. Neher, L. Korte, M. Stolterfoht, S. Albrecht, *Adv. Mater.* **2024**, *8*, 2307743.
[26] J. Zheng, W. Duan, Y. Guo, Z. C. Zhao, H. Yi, F.-J. Ma, L. Granados Caro, C. Yi, J. Bing, S. Tang, J. Qu, K. C. Fong, X. Cui, Y. Zhu, L. Yang, A. Lambertz, M. Arafat Mahmud, H. Chen, C. Liao, G. Wang, M. Jankovec, C. Xu, A. Uddin, J. M. Cairney, S. Bremner, S. Huang, K. Ding, D. R. McKenzie, A. W. Y. Ho-Baillie, *Energy Environ. Sci.* **2023**, *16*, 1223.
[27] J. Zheng, C. Xue, G. Wang, M. A. Mahmud, Z. Sun, C. Liao, J. Yi, J. Qu, L. Yang, L. Wang, S. Bremner, J. M. Cairney, J. Zhang, A. W. Y. Ho-Baillie, *ACS Energy Lett.* **2024**, *9*, 1545.
[28] Y.-H. Chiang, K. Frohna, H. Salway, A. Abfalterer, L. Pan, B. Roose, M. Anaya, S. D. Stranks, *ACS Energy Lett.* **2023**, *8*, 2728.
[29] R. Singh, S. K. Mukherjee, *J. Mater. Sci. Mater. Electron.* **2022**, *33*, 6969.
[30] A. V. Singh, R. M. Mehra, N. Buthrath, A. Wakahara, A. Yoshida, *J. Appl. Phys.* **2001**, *90*, 5661.
[31] V. O. Anyanwu, M. K. Moodley, *Ceram. Int.* **2023**, *49*, 5311.
[32] S. J. Kang, Y. H. Joung, *J. Mater. Sci. Mater. Electron.* **2013**, *24*, 1863.
[33] D. H. A. Blank, M. Dekkers, G. Rijnders, *J. Phys. D. Appl. Phys.* **2014**, *47*, 034006.
[34] Y. Smirnov, P.-A. Repecaud, L. Tutsch, I. Florea, K. P. S. Zanoni, A. Paliwal, H. J. Bolink, P. R. i Cabarrocas, M. Bivour, M. Morales-Masis, *Mater. Adv.* **2022**, *3*, 3469.
[35] K. P. S. Zanoni, A. Paliwal, M. A. Hernández-Fenollosa, P. Repecaud, M. Morales-Masis, H. J. Bolink, *Adv. Mater. Technol.* **2022**, *7*, 2101747.
[36] K. P. S. Zanoni, D. Pérez-del-Rey, C. Dreessen, N. Rodkey, M. Sessolo, W. Soltanpoor, M. Morales-Masis, H. J. Bolink, *ACS Appl. Mater. Interfaces.* **2023**, *15*, 32621.
[37] O. Lupan, S. Shishiyanu, V. Ursaki, H. Khallaf, L. Chow, T. Shishiyanu, V. Sontea, E. Monaico, S. Railean, *Sol. Energy Mater. Sol. Cells.* **2009**, *93*, 1417.
[38] Q. Nian, K. H. Montgomery, X. Zhao, T. Jackson, J. M. Woodall, G. J. Cheng, *Appl. Phys. A.* **2015**, *121*, 1219.
[39] R. Pietruszka, B. S. Witkowski, S. Gieraltowska, P. Caban, L. Wachnicki, E. Zielony, K. Gwozdz, P. Bieganski, E. Placzek-Popko, M. Godlewski, *Sol. Energy Mater. Sol. Cells.* **2015**, *143*, 99.
[40] N. Li, F. Meng, F. Huang, G. Yu, Z. Wang, J. Yan, Y. Zhang, Y. Ai, C. Shou, Y. Zeng, J. Sheng, B. Yan, J. Ye, *ACS Appl. Energy Mater.* **2020**, *3*, 9610.
[41] D. Zhang, W. Yu, L. Zhang, X. Hao, *Materials.* **2023**, *16*, 5537.
[42] G. Dong, J. Li, Y. Zhao, X. Ran, C. Peng, D. He, C. Jin, Q. Wang, H. Jiang, Y. Zhang, X. Cao, C. Yu, *Prog. Photovolt. Res. Appl.* **2023**, *31*, 931.
[43] Q. Wei, Z. Yang, D. Yang, W. Zi, X. Ren, Y. Liu, X. Liu, J. Feng, S. (Frank) Liu, *Sol. Energy.* **2016**, *135*, 654.
[44] A. Baltakesmez, M. Biber, S. Tüzemen, *J. Radiat. Res. Appl. Sci.* **2018**, *11*, 124.
[45] Z.-L. Tseng, C.-H. Chiang, S.-H. Chang, C.-G. Wu, *Nano Energy.* **2016**, *28*, 311.
[46] T. Nakamura, E. Matsubara, N. Sato, A. Muramatsu, H. Takahashi, *Mater. Trans.* **2004**, *45*, 2068.
[47] H. Usui, O. Miyamoto, T. Nomiyama, Y. Horie, T. Miyazaki, *Sol. Energy Mater. Sol. Cells.* **2005**, *86*, 123.
[48] F. K. Shan, B. C. Shin, S. W. Jang, Y. S. Yu, *J. Eur. Ceram. Soc.* **2004**, *24*, 1015.
[49] G. Kaur, A. Mitra, K. L. Yadav, *Prog. Nat. Sci. Mater. Int.* **2015**, *25*, 12.
[50] K. C. Park, D. Y. Ma, K. H. Kim, *Thin Solid Films.* **1997**, *305*, 201.
[51] H. Kim, A. Piqué, J. . Horwitz, H. Murata, Z. . Kafafi, C. . Gilmore, D. . Chrisey, *Thin Solid Films.* **2000**, *377*, 798.
[52] Z. Qiao, C. Agashe, D. Mergel, *Thin Solid Films.* **2006**, *496*, 520.
[53] S. W. Xue, X. T. Zu, W. G. Zheng, H. X. Deng, X. Xiang, *Phys. B Condens. Matter.* **2006**, *381*, 209.
[54] Q. H. Li, D. Zhu, W. Liu, Y. Liu, X. C. Ma, *Appl. Surf. Sci.* **2008**, *254*, 2922.
[55] C.-H. Zhai, R.-J. Zhang, X. Chen, Y.-X. Zheng, S.-Y. Wang, J. Liu, N. Dai, L.-Y. Chen, *Nanoscale Res. Lett.* **2016**, *11*, 407.
[56] K. P. S. Zanoni, L. Martínez-Goyeneche, C. Dreessen, M. Sessolo, H. J. Bolink, *Sol. RRL.* **2023**, *7*, 2201073.
[57] M. Piot, J. E. S. Alonso, K. P. S. Zanoni, N. Rodkey, F. Ventosinos, C. Roldán-Carmona, M. Sessolo, H. Bolink, *ACS Energy Lett.* **2023**, *8*, 4711.
[58] A. Paliwal, K. P. S. Zanoni, C. Roldán-Carmona, M. A. Hernández-Fenollosa, H. J. Bolink, *Matter.* **2023**, *6*, 3499.
[59] N. Rodkey, K. P. S. Zanoni, M. Piot, C. Dreessen, R. Grote, P. Carroy, J. E. Sebastian Alonso, A. Paliwal, D. Muñoz, H. J. Bolink, *Adv. Energy Mater.* **2024**, *14*, 2400058.
[60] A. Paliwal, K. P. S. Zanoni, C. Roldan, N. Rodkey, H. J. Bolink, *ACS Energy Lett.* **2024**, *9*, 4587.
[61] S. J. Byrnes, https://doi.org/10.48550/arXiv.1603.02720.
[62] I. C. Kaya, K. P. S. Zanoni, F. Palazon, M. Sessolo, H. Akyildiz, S. Sonmezoglu, H. J. Bolink, *Adv. Energy Sustain. Res.* **2021**, *2*, 2000065.
[63] V. Linseis, F. Völklein, H. Reith, K. Nielsch, P. Woias, *Rev. Sci. Instrum.* **2018**, *89*, 015110.